iScience

CellPress
OPEN ACCESS

Article

Liquid metal motor

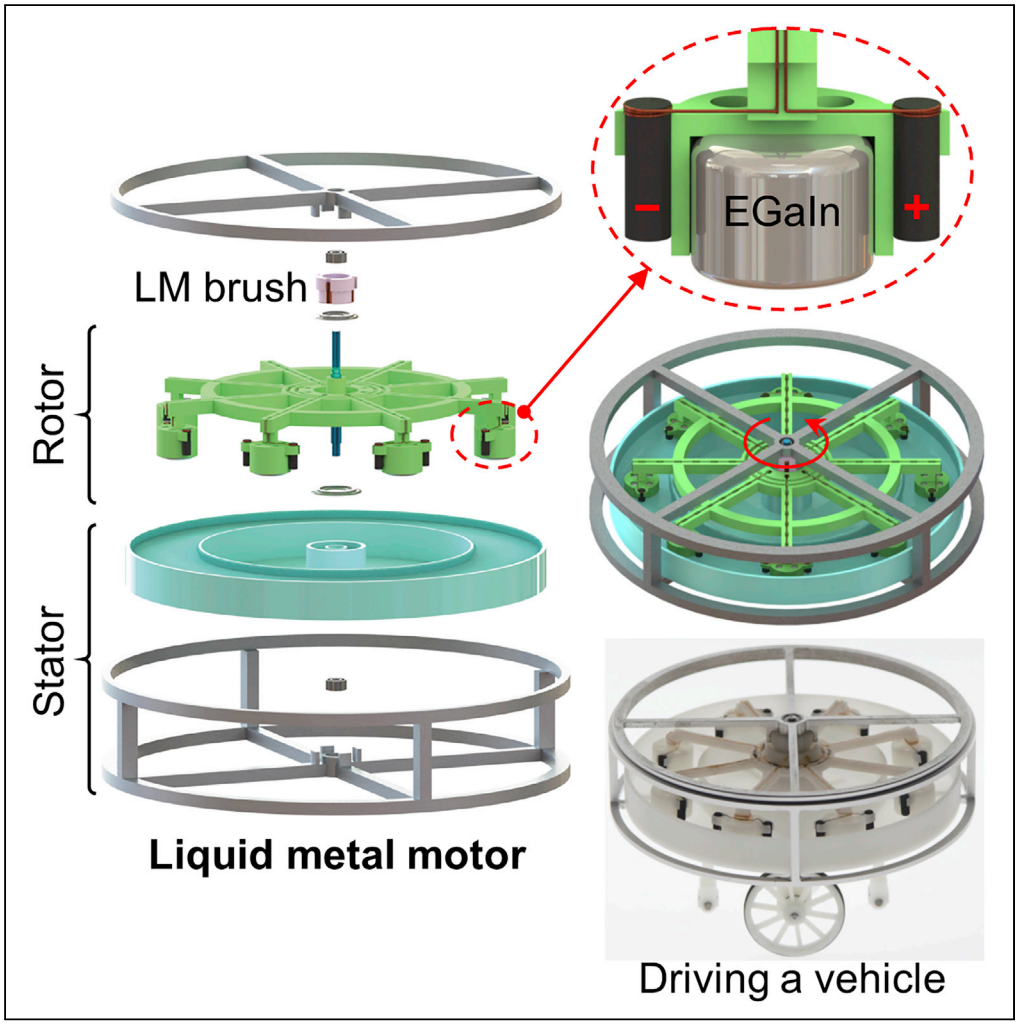

Erlong Wang, Jian Shu, Hu Jin, ..., Weihua Li, Michael D. Dickey, Shiwu Zhang

s.tang@bham.ac.uk (S.-Y.T.)
licool@suda.edu.cn (X.L.)
swzhang@ustc.edu.cn (S.Z.)

HIGHLIGHTS

The motor is driven by liquid metal droplets without using conventional electromagnets

The liquid metal enabled solid-liquid contact brush provides low friction and low wear

The liquid metal motor can be readily adapted to drive various untethered vehicles

Wang et al., iScience 24, 101911
January 22, 2021
https://doi.org/10.1016/j.isci.2020.101911

iScience

CellPress
OPEN ACCESS

Article

Liquid metal motor

Erlong Wang,[1,7] Jian Shu,[1,7] Hu Jin,[1,7] Zhe Tao,[1] Jie Xie,[1] Shi-Yang Tang,[2,*] Xiangpeng Li,[3,4,*] Weihua Li,[5] Michael D. Dickey,[6] and Shiwu Zhang[1,8,*]

Summary

Liquid metal has demonstrated an enormous potential for developing soft functional devices and machines. However, current liquid metal enabled machines suffer from several issues, such as the requirement of a liquid environment, generation of weak actuating forces, and insufficient maneuverability. To overcome these restrictions, here, a motor is developed based on the electrical actuation of liquid metal droplets without the need for conventional electromagnets. The approach is distinguished by (1) the encapsulation of electrolyte and multiple liquid metal droplets within an enclosed system, and (2) the creation of stable and continuous torque outside a liquid environment. In addition, a liquid metal electrical brush is introduced to operate the motor with low friction and low wear. The unique driving mechanism endows the motor with several advantages, including low friction, no sparking, low noise, versatile working environment, and being built from soft materials that could offer new opportunities for developing soft robotics.

Introduction

Devices powered by soft machines have tremendous potential in bridging the gap between the soft materials found in life sciences and the (often) stiff material used in engineering (Cacucciolo et al., 2019). Numerous biomimetic robotic systems such as insect-inspired robots, soft grippers, and underwater robots have been explored to perform tasks using elastomers (Christianson et al., 2018; Rafsanjani et al., 2018), stimuli-response gels/hydrogels (Banerjee and Ren, 2017; Li et al., 2017), liquid crystals (Camacho-Lopez et al., 2004; Palagi et al., 2016), shape-memory polymers (Fan and Li, 2017), and other flexible or stretchable materials (Laschi et al., 2016; Yang et al., 2019).

In recent years, room temperature liquid metals have enabled unique opportunities to be used as the core of machines. Gallium-based liquid metals such as EGaIn (75 wt% gallium, 25 wt% indium) and Galinstan (68.5 wt% gallium, 21.5 wt% indium, 10 wt% tin) possess many excellent properties such as high electrical and thermal conductivities, low viscosity, high surface tension, and most importantly, much lower toxicity compared to mercury (Dickey, 2017). Liquid metals have the largest interfacial tension (>400 mN/m) of any liquid or soft material. The ability to use electricity to tune the interfacial tension provides an opportunity to create gradients or step changes in this force, and thus, convert electrical energy into mechanical energy. Continuous electrowetting (CEW) uses these principles to drive Marangoni flow of fluids within electrolytes (Eaker and Dickey, 2016; Lee and Kim, 2000; Tang et al., 2013a). This type of actuation cannot be realized with any other soft materials, making liquid metals stand out among conventional soft matter.

Until now, electrification of liquid metal has been used almost exclusively to move fluids within otherwise static devices or within electrolytes. For example, CEW has been employed to make pumps(Tang et al., 2014a), mixers(Tang et al., 2014b), microactuators(Khoshmanesh et al., 2017; Li et al., 2020), and tunable antennas(Reichel et al., 2018; Wang et al., 2015), Liquid metals have also been moved using dynamic magnetic fields to induce a Lorentz force(Shu et al., 2018; Yu and Miyako, 2018), chemical reactions to induce unbalanced surface tension (Shu et al., 2020; Tang et al., 2013b; Zhang et al., 2015), electrostatic force (Zhang et al., 2019b), and ultrasound generated acoustic radiation force (Wang et al., 2018).

Although there are many ways to move liquids via forces from electrokinetic or electromagnetic phenomena, there are almost no examples that can drive motors and provide a useful output torque. Liquid metal is a sensible candidate due to its electrical conductivity, low viscosity, and large tension. Nonetheless, liquid

[1]CAS Key Laboratory of Mechanical Behavior and Design of Materials, Department of Precision Machinery and Precision Instrumentation, University of Science and Technology of China, Hefei 230026, China

[2]Department of Electronic, Electrical and Systems Engineering, University of Birmingham, Edgbaston, Birmingham, B15 2TT, UK

[3]College of Mechanical and Electrical Engineering, Soochow University, Suzhou 215000, China

[4]State Key Laboratory of Applied Optics, Changchun Institute of Optics, Changchun 130033, China

[5]School of Mechanical, Materials, Mechatronic and Biomedical Engineering, University of Wollongong, Wollongong, NSW 2500, Australia

[6]Department of Chemical and Biomolecular Engineering, North Carolina State University, Raleigh, NC 27695, USA

[7]These authors contributed equally

[8]Lead contact

*Correspondence: s.tang@bham.ac.uk (S.-Y.T.), licool@suda.edu.cn (X.L.), swzhang@ustc.edu.cn (S.Z.)

https://doi.org/10.1016/j.isci.2020.101911

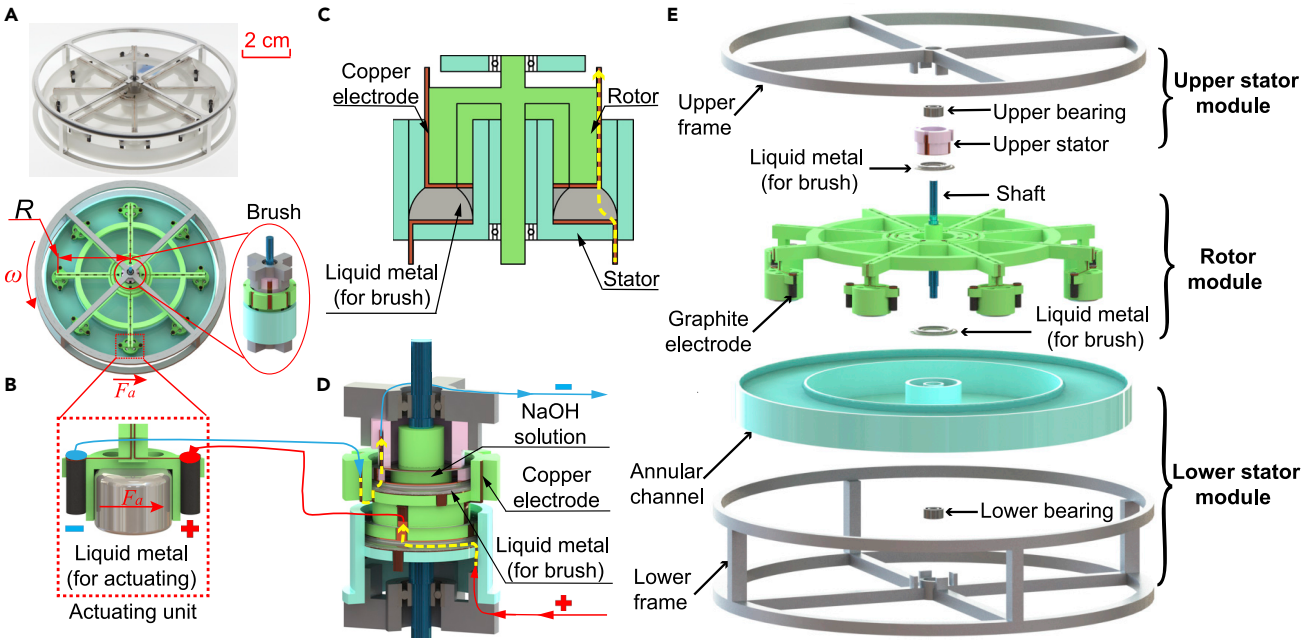

Figure 1. Design of the liquid metal motor

(A) Photograph and schematic of the liquid metal motor.

(B–D) (B) Schematic of a single actuating unit. Schematics showing the working mechanism of (C) a single and (D) two liquid metal-based solid-liquid contact brushes.

(E) Explosion view of the liquid metal motor, the torque generated by the rotor is transmitted to gears via the shaft.

metal enabled motors with the ability to provide stable and useable torque have not been realized to date due to several drawbacks (Tan et al., 2015b; Xu et al., 2019). For instance, previously reported motor-like devices only rotate liquid metal droplets or slugs in a groove without a proper method to connect it to a shaft for transmitting the produced torque (Lee and Kim, 2000; Tan et al., 2015a). Liquid metal droplets powered by the CEW effect must also be submerged within a solution for two reasons. First, liquid metals based on gallium for a native oxide that causes the metal to adhere to surfaces. Strong base or acid (or acidified siloxane oils) is generally needed to constantly remove the native gallium oxide layer formed on the surface of liquid metal (Holcomb et al., 2016). Second, the principles of CEW rely on the electric double layer that forms between the metal and electrolyte. Despite these limitations, we have previously demonstrated a wheeled robot which utilizes a liquid metal droplet to induce locomotion outside a liquid environment by constantly altering the robot's center of gravity in a 'hamster wheel' device (Wu et al., 2018). However, the weak actuating force provided by a single droplet and its low maneuverability limit this approach. Thus, there is a need to find an approach that can harness the simplicity of using liquid metal to drive motors.

Harnessing the unique properties of liquid metal, this work offers a new way to convert electrical energy to useful mechanical torque without the use of conventional mechanisms (electromagnetic, electrostatic, or magnetohydrodynamic forces). The resulting liquid metal motor uses interfacial tension to drive motors in a revolving manner, whereas to date, interfacial tension has mostly been utilized to drive liquid movement within an electrolyte environment without the ability to provide a useful torque. Such a motor has an enclosed system that contains multiple liquid metal droplets as the rotor for providing a stable and continuous output torque. Each liquid metal droplet is confined within a chamber to act as the actuating unit of the rotor, and each droplet is controlled by a pair of electrodes, as shown in Figure 1. By harnessing the high electrical conductivity and low viscosity of liquid metal, we designed a novel solid-liquid contact brush that greatly reduces the friction between the rotor and stator. Unlike conventional brush-motors, there is no concern with wear nor sparking in the all-liquid environment. We investigated further the parameters affecting the actuating force of a single actuating unit and the rotational speed of the motor. Finally, we applied the liquid metal motor to drive untethered vehicles and boats to demonstrate the versatility and maneuverability of the motor.

Results and discussion

Figure 1A shows the photograph and schematic of the assembled liquid metal motor. The motor consists of four major parts: a motor rotor, two liquid metal enabled solid-liquid contact brushes, an annular channel, and a frame. The role of each part is given below:

Motor rotor

The frame of the motor rotor has several chambers for confining the liquid metal droplets, which are used as actuators, as shown in Figure 1B. The output shaft is fixed on the motor rotor. When actuated, the output shaft rotates with the rotor and transfer the torque to external element.

Solid-liquid contact brushes

We applied two solid-liquid contact brushes enabled by liquid metal to connect the positive and negative poles of the power supply to the actuating unit to avoid entanglement of wires (Figure 1B). Figures 1C and 1D show the direction of current passing through the brushes.

Annular channel

The annular channel accommodates the actuating units of the motor rotor (Figure 1E). We filled the channel with sodium hydroxide (NaOH) solution and liquid metal droplets within the motor rotor were immersed in the solution.

Motor frame

The motor frame consists an upper and a lower frame (see Figure 1E). We used the frame to support the rotor and the annular channel.

A pair of graphite electrodes connected to an external power source are mounted outside each chamber for activating the liquid metal droplets. When we apply a DC voltage to the electrodes, the potential gradient between the electrodes induces an imbalance of interfacial tension along the surface of liquid metal droplets (Tang et al., 2014a; Zhang et al., 2015). This imbalance propels the droplet toward the anode (Tang et al., 2014a; Tang et al., 2014c).

In conventional electric motors, the coils of the rotor must be connected to complete an electrical circuit. "Brushes"—spring-mounted electrodes that contact other moving electrodes—conduct current between the rotating rotor and the stationary stator to avoid wire entanglement. Common solid-solid contact brushes have various inevitable drawbacks such as relatively large friction, material wear, sparking, and small contact area. These factors can result in poor connection of circuit and short life span of a brush. The solid-liquid contact brush used here has none of these issues. Figure 1C depicts the working mechanism of the solid-liquid brush. The stator and the rotor are each covered by a layer of copper electrode. A ring of liquid metal connects these two electrodes. As such, the liquid metal ring can conduct current and allow for the free rotation of the rotor.

Figure 2A shows the explosion view of the solid-liquid contact brush used in the liquid metal motor. Instead of using one liquid metal ring, we adopted two rings to isolate the rotor from the upper and the lower stators. In doing so, the graphite electrodes can be connected to the DC power source *via* the liquid metal rings without affecting the rotational movement of the rotor. We added a few drops of NaOH solution to the solid-liquid brushes to keep the liquid metal free of oxide. To ensure electrical contact and avoid oxidation between the liquid metal and the copper electrodes, we electrochemically treated the surface of the copper electrodes with liquid metal (see Figure S1 for details). This allows the formation of a thin $CuGa_2$ layer on the surface of copper electrode to significantly improve its wettability to liquid metal, making the liquid metal adhere to the copper electrode (Zhang et al., 2019a). Moreover, the formation of intermetallic compound $CuGa_2$ with a strong interaction could help prevent the electrodes being further corroded and ensure the connection of the circuit (Cui et al., 2018; Shu et al., 2020). Compared to solid-solid contact brushes with different diameters, due to the high electrical conductivity of liquid metal and the negligible internal sliding friction induced by its low viscosity, the solid-liquid contact brush can provide extremely low friction that is one order of magnitude less than that of conventional solid-solid contact brush, as shown in Figure 2B. It should be noted that there are actually three layers of liquid metal in the

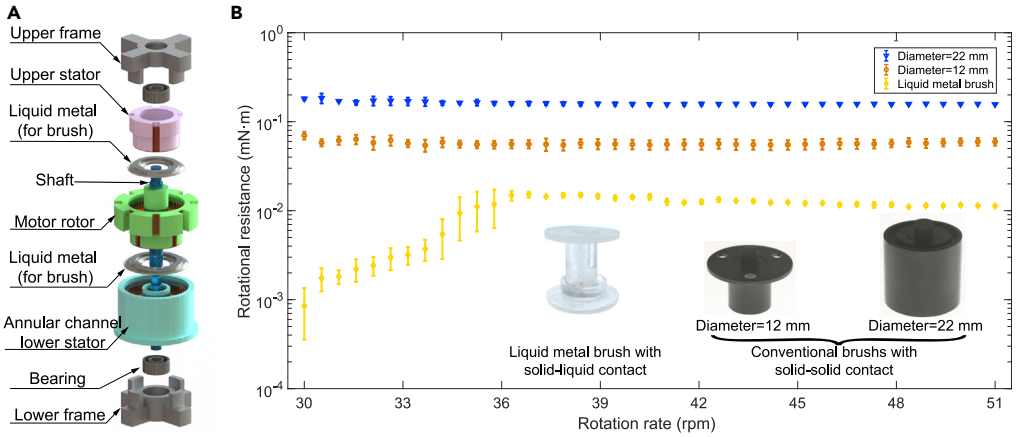

Figure 2. Solid-liquid contact brush in the liquid metal motor

(A) Explosion view of the solid-liquid contact brush used in liquid metal motor.

(B) Plots of rotational resistance vs. rotational speed of different types of brushes. Data are represented as mean ± standard deviation (SD).

motor. Two layers acts as a brush, the other are droplets and acts to generate force. The animation of the assembling process of the liquid metal motor is given in Video S1.

After developing the platform, we investigated the dynamics of the operation of the motor. When the motion of the droplet is hindered by the chamber, the chamber will be subjected to a thrust F_a (Figure 1A), which can be expressed as (Li et al., 2019; Xie et al., 2018, 2020; Yao and Liu, 2016):

$$F_a = \pi q_0 I R_p H \frac{\Phi}{2} \quad \text{(Equation 1)}$$

where q_0 is total charges per unit area of the EDL, I denotes the current through the electrolyte, R_p is the resistance per unit length of the thin electrolyte layer between the liquid metal droplet and the chamber wall, and H and Φ are the height and the diameter of the liquid metal droplet, respectively. Notably, the current I is proportional to voltage U.

Considering the chamber and the liquid metal droplet together as a single actuating unit, it also experiences the viscous resistance F_v from the solution and the friction f between the liquid metal droplet and the channel, where F_v and f can be expressed as:

$$F_v = c_r \cdot (\omega R)^2 \quad \text{(Equation 2)}$$

$$f = \mu \pi g H \cdot (\rho_l - \rho_s) \left(\frac{\Phi}{2}\right)^2 \quad \text{(Equation 3)}$$

where c_r is the coefficient of viscous resistance of rotor, ω is the rotating speed of the motor, R is radius of chamber rotation, μ is the coefficient of friction between liquid metal and substrate in solution, and ρ_l, ρ_s are the densities of liquid metal and NaOH solution, respectively. In addition to F_v and f, the rotor also experience a resistance caused by the solid-liquid contact brush, F_b which can be expressed as:

$$F_b = c_b \cdot (\omega R_b)^2 \quad \text{(Equation 4)}$$

where c_b is the coefficient of viscous resistance of the brush, and R_b is the equivalent radius of the brush. The resultant force propels the rotor, to drive the output shaft fixed at the center of the rotor. Neglecting the small friction of the bearing rotation, the torque balance equation of the liquid metal motor can be expressed as:

$$n(F_a - F_v - f)R - 2F_b R_b = I\dot{\omega} \quad \text{(Equation 5)}$$

where n is the number of actuating units, and I is the rotational inertia of the motor.

Perhaps more importantly, unlike conventional motors in which overheating or even break down may occur when the rotor is locked under special circumstances, the unique configurations of the liquid metal motor ensure an excellent stability and safety during operation.

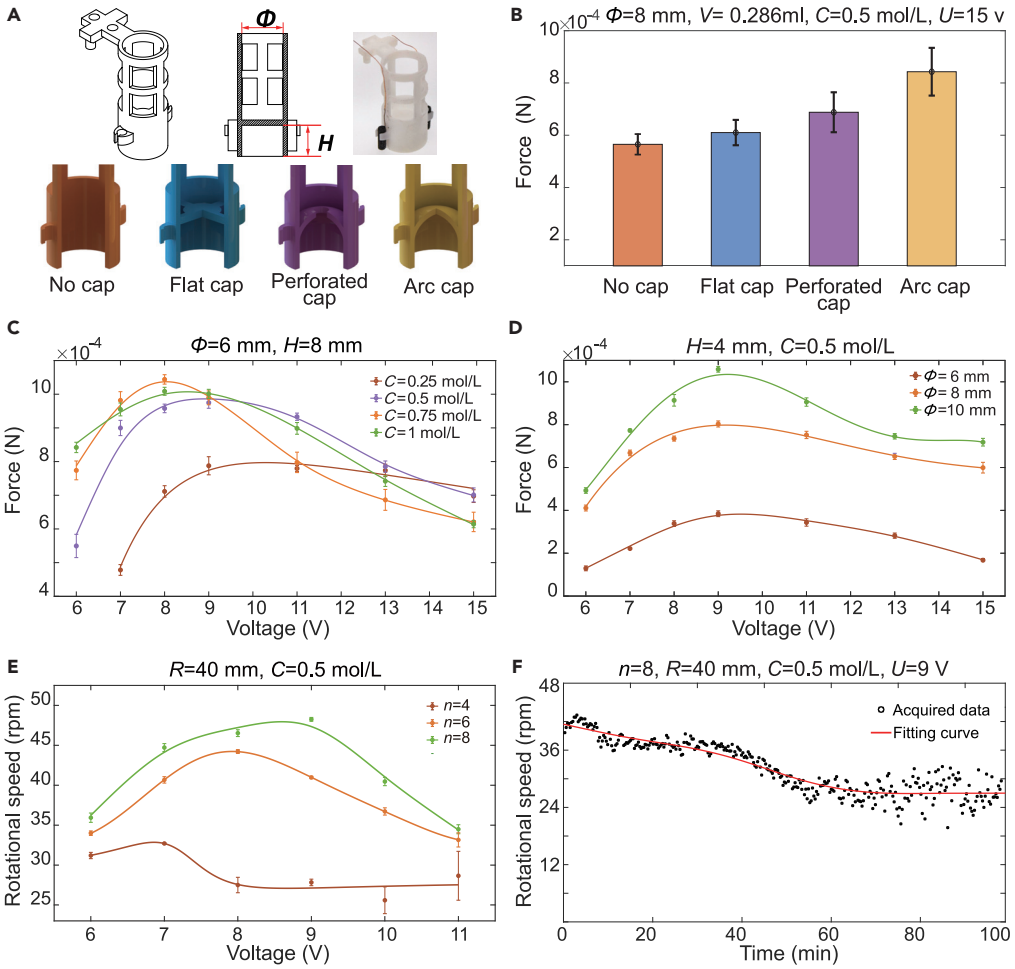

Figure 3. Characterization of the driving performance with respect to different parameters

(A) Schematic and photograph of the droplet chamber with different cap shapes, where *H* is the height of liquid metal droplet and *Φ* is the diameter of the cylinder.

(B) Plots of actuating force vs. shape of the chamber.

(C) Plots of actuating force vs. voltage; brown, purple, orange, and green curves indicate different concentrations of NaOH solution.

(D) Plots of actuating force vs. voltage; brown, orange, and green curves indicate different diameters of the liquid metal droplets.

(E) Plots of no-load speed of liquid metal motor vs. voltage; brown, orange, and green curves indicate different numbers of actuating unit.

(F) Plots of rotational speed vs. time over a course of 100 min. In B, C, D, and E, data are represented as mean ± SD.

From Equation 5, we can see that the thrust F_a and the number of the actuating units n can significantly affect the performance of the motor. Interestingly, we found that the shape of the chamber also can affect the thrust F_a exerted on the actuating unit. In order to characterize the influence of chamber shape on the thrust, we designed a system to measure the actuating force F_a, as detailed in Figure S2. Figure 3A shows the schematic and photograph of the 3D printed chamber. We designed four chambers with or without caps, which are denoted as *no cap*, *flat cap*, *perforated cap*, and *arc cap*.

We conducted a series of experiments to investigate the actuating performance of the rotor as a function of the cap shape of the chambers, the supplied voltage, the concentration of NaOH solution, the height of liquid metal droplets, as well as the diameter of the chambers, as summarized in Figure 3. Our experiments show that the chamber with an arc cap provides the largest actuating force, followed by the chambers with perforated arc cap and flat cap; the chamber without a cap provides the least actuating force, as shown in

Figure 3B. For the extreme situation which the difference in interfacial tension reaches the limit of ~500 mN/m, the theoretical maximum driving force exerted on a spherical droplet with a diameter of 8 mm is ~12.56 mN, indicating that our measured driving forces per droplet within a range between 2.5 and 4.5 mN is reasonable. Interestingly, we observed that during the actuation, the droplet pumped the solution upwards along the chamber under the Marangoni effect (Figure S3). Actuating unit with a sealed cap can redirect the flow of the solution to enhance the thrust, which is beneficial for improving the actuating performance of the unit. On the other hand, for sealed chambers (such as the chamber with an arc cap), gas bubbles generated by electrolysis can be driven by the Marangoni flow to enter the chamber. This could cause the liquid metal droplet to be pushed out of the chamber from the gap between the chamber bottom and the substrate, making the driving process unstable. Considering the trade-off between the actuating force and stability, we adopt the chamber with a flat cap for making the actuating unit.

We next investigated the effect of the applied voltage U on the thrust of the actuating unit, as show in Figure 3C. The actuating unit cannot overcome the friction until the voltage reaches about 6 V in 0.5 mol/L NaOH solution. When the voltage is less than 8 V, the actuating force of liquid metal droplet increases as the increase in voltage, however, the actuating force decreases gradually when the voltage exceeds 9 V. According to Equation 1, the increase in voltage should induce a larger actuating force, however, this also induces undesired electrolysis of the solution, which may weaken the driving performance of liquid metal. Figure 3C also shows that the concentration of NaOH solution C can affect the actuating performance. When C increases from 0.25 to 0.5 mol/L, the critical voltage required for driving the unit dropped from 7 to 6 V. In addition, a larger actuating force can be achieved by increasing the concentration of NaOH solution. However, no further increase of force was observed when C is higher than 0.75 mol/L. The performance of the motor with multiple actuating units is similar to the case of the single actuating unit, as detailed in Figure S4. Furthermore, we investigated the effect of the diameter Φ of the liquid metal droplet on the actuating force, as shown in Figure 3D (the effect of the droplet height H is also studied and shown Figure S5). We found that liquid metal droplets with larger size can produce a stronger actuating force, which is also in line with Equation 1. Actuating forces in different liquid metal droplet diameters also decrease as the voltage increases due to the more intense electrolysis when the voltage exceeds 9 V.

After exploring the parameters affecting the thrust produced by a single actuating unit, we next investigated the actuating performance of the assembled motor with multiple actuating units. From Equation (5), we can see that increasing the number of actuating unit n can result in a faster rotational speed of the motor. We examined this by integrating four, six, and eight actuating units into the motor and recorded the rotational speed of the rotor, as shown in Figure 3E. We chose the no-load condition to characterize the motor performance, and it is clear that more actuating units can lead to a higher rotational speed and a more stable operation of the rotor.

We further examined the long-term performance of the liquid metal motor by continuously operating the motor and monitoring the speed of rotation, as shown in Figure 3F. The motor is capable of working unceasingly for at least ~100 min with the rotating speed steadily decrease until the hardware fails. We observed the gradual decomposition of the graphite electrodes caused by electrolysis. This may cause the decrease in current, thereby reducing the actuating force and motor speed. Hardware failure may eventually occur when the wires connected to the graphite electrodes fall off.

After examining the parameters affecting the performance of the liquid metal motor, we further applied the motor to drive machines including untethered vehicle and boat, as shown in Figure 4. Figures 4A and 4C, respectively, show the vehicle and the boat with integrated liquid metal motors. We fixed a spur gear on the output shaft of the liquid metal motor to drive the crown wheel, and this converts the rotation of the motor into the actuation of the vehicle wheels or boat spindles. Integrated wireless module was used to remotely control the locomotion of the vehicle and boat. The total weight of the vehicle and boat with battery and control modules is about 78 g and 121 g, respectively. By controlling the voltage and current direction of the liquid metal motor, the starting, stopping, forward and backward locomotion of the vehicle and boat can be realized, as shown in Figures 4B and 4D (also see Video S2). The average forward speed and backward speed of the vehicle is 2.1 and 1.6 cm/s, respectively. We envisage that multiple liquid metal motors can be assembled in series and parallel to construct more complex systems.

Conclusions

In summary, this paper demonstrates a liquid metal motor based on the electrical actuation of liquid metal droplets. Unlike any previously reported liquid metal actuators, this motor can be readily integrated to

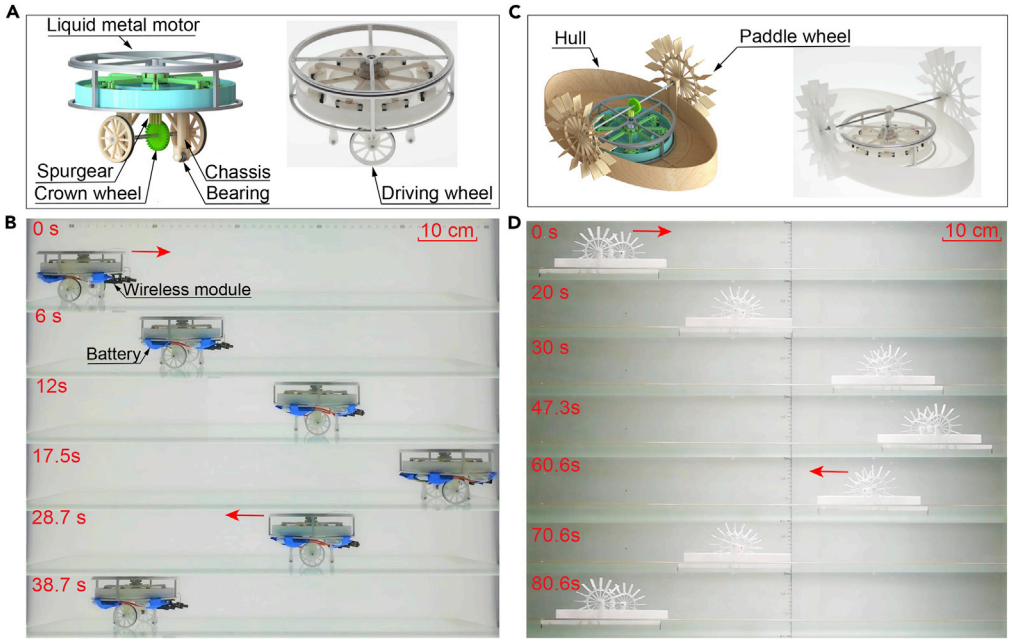

Figure 4. Vehicle and boat driven by liquid metal motors

(A) Schematic and photograph of the untethered vehicle.

(B) Sequential snapshots of the forward and backward locomotion of the untethered vehicle.

(C) Schematic and photograph of untethered boat.

(D) Sequential snapshots of the forward and backward locomotion of the untethered boat.

other systems and is capable of providing a stable and relatively large torque to continuously drive machines outside a liquid environment. Moreover, we demonstrated a solid-liquid contact brush with the incorporation of liquid metal to conduct current in the liquid metal motor. Compared to conventional solid-solid contact, this brush can reduce friction and material wear during the operation of the motor. We thoroughly explored the parameters affecting the performance of the motor. More importantly, due to the simplicity and excellent versatility and maneuverability of the motor, we integrated the motor into other machines and demonstrated the remotely controlled actuation of an untethered vehicle and boat. Such a motor could be further adopted to drive underwater actuating systems or perhaps be integrated into systems constructed from a greater portion of soft materials. Although conventional electric motors can generate larger torques and higher rotating speeds, the liquid metal motor developed in this work enables the possibility of using soft materials to provide stable and continuous torque to drive machines, which also possesses several advantages such as simple fabrication, easy maintenance, and relatively low cost. Perhaps more importantly, the liquid metal motor has the ability to avoid the safety hazards caused by the rotor blocking, which is a risky problem for conventional electric motors. We believe the developed liquid metal motor possesses tremendous application potentials in the fields of soft electronics, soft robotics, microelectromechanical systems, and microfluidics.

Limitations of the study

Electrical actuation of liquid metal droplets generates hydrogen and oxygen bubbles due to the electrolysis of solution. This could affect the stability of operation. However, the applied voltage is relatively small, and the volume of gas generated is also small; therefore, the gas is not a safety hazard when the system is not completely sealed. An alternative approach to solve this problem is to apply an AC voltage with a DC offset for reducing electrolysis (Tang et al., 2014b). In addition, the rotational speed of the liquid metal motor is determined by the locomotion speed of liquid metal droplets, which is relatively low compared to the speed of conventional motor rotors. Meanwhile, the actuating force of the liquid metal motor is relatively small compared to conventional electric motors with a similar weight. The liquid metal motor with a mass of 20 g (excluding the frames) provides a torque of 0.0264 mN·m, while commercial DC motors can reach a torque of 1.52 mN·m (e.g. RE 16 Φ16 mm, Precious Metal Brushes CLL, MAXON, Switzerland).

Resource availability

Lead contact

Further information and requests for resources and reagents should be directed and will be fulfilled by the Lead Contact, Shiwu Zhang (swzhang@ustc.edu.cn).

Materials availability

This study did not generate new unique reagents.

Data and code availability

This study did not generate/analyze dataset/code.

Methods

All methods can be found in the accompanying Transparent Methods supplemental file.

Supplemental information

Supplemental Information can be found online at https://doi.org/10.1016/j.isci.2020.101911.

Acknowledgments

This research has been partially supported by the National Natural Science Foundation of China (No. 51975550, 51828503, U1713206, 61503270). X.L. is supported in part by a grant from NSFC under Grant No. 61873339, a grant from China Postdoctoral Science Foundation under Grant No. 2016M590497, a grant from National Science Foundation of Jiangsu Province under Grant No. BK20190096, and supported by the State Key Laboratory of Applied Optics. The authors declare no competing interest.

Author contributions

E.W., J.S. and H.J. contributed equally to this work. S.Z., S.-Y.T, and X.L. designed research; E.W., J.S., H.J, Z.T., and J.X. performed research; E.W., J.S., H.J, Z.T., J.X., S.-Y.T, X.L., M.D.D., and S.Z. analyzed data; E.W., J.S., H.J, S.-Y.T, X.L., M.D.D., and S.Z. wrote the paper; and S.-Y.T, X.L., and S.Z. supervised the experimental analysis.

Declaration of interests

The authors declare that they have no conflict of interest.

Received: September 14, 2020
Revised: November 4, 2020
Accepted: December 3, 2020
Published: January 22, 2021

References

Banerjee, H., and Ren, H.L. (2017). Optimizing double-network hydrogel for biomedical soft robots. Soft Robot *4*, 191–201.

Cacucciolo, V., Shintake, J., Kuwajima, Y., Maeda, S., Floreano, D., and Shea, H. (2019). Stretchable pumps for soft machines. Nature *572*, 516–519.

Camacho-Lopez, M., Finkelmann, H., Palffy-Muhoray, P., and Shelley, M. (2004). Fast liquid-crystal elastomer swims into the dark. Nat. Mater. *3*, 307–310.

Christianson, C., Goldberg, N.N., Deheyn, D.D., Cai, S.Q., and Tolley, M.T. (2018). Translucent soft robots driven by frameless fluid electrode dielectric elastomer actuators. Sci. Robot. *3*, eaat1893.

Cui, Y.T., Liang, F., Yang, Z.Z., Xu, S., Zhao, X., Ding, Y.J., Lin, Z.S., and Liu, J. (2018). Metallic bond-enabled wetting behavior at the liquid Ga/CuGa2 interfaces. ACS Appl. Mater. Interfaces *10*, 9203–9210.

Dickey, M.D. (2017). Stretchable and soft electronics using liquid metals. Adv. Mater. *29*, 1606425.

Eaker, C.B., and Dickey, M.D. (2016). Liquid metal actuation by electrical control of interfacial tension. Appl. Phys. Rev. *3*, 031103.

Fan, J., and Li, G. (2017). High performance and tunable artificial muscle based on two-way shape memory polymer. RSC Adv. *7*, 1127–1136.

Holcomb, S., Brothers, M., Diebold, A., Thatcher, W., Mast, D., Tabor, C., and Heikenfeld, J. (2016). Oxide-free actuation of gallium liquid metal alloys enabled by novel acidified siloxane oils. Langmuir *32*, 12656–12663.

Khoshmanesh, K., Tang, S.Y., Zhu, J.Y., Schaefer, S., Mitchell, A., Kalantar-Zadeh, K., and Dickey, M.D. (2017). Liquid metal enabled microfluidics. Lab Chip *17*, 974–993.

Laschi, C., Mazzolai, B., and Cianchetti, M. (2016). Soft robotics: technologies and systems pushing the boundaries of robot abilities. Sci. Robot. *1*, eaah3690.

Lee, J., and Kim, C.J. (2000). Surface-tension-driven microactuation based on continuous electrowetting. J. Microelectromech. Syst. *9*, 171–180.

Li, T.F., Li, G.R., Liang, Y.M., Cheng, T.Y., Dai, J., Yang, X.X., Liu, B.Y., Zeng, Z.D., Huang, Z.L., Luo, Y.W., et al. (2017). Fast-moving soft electronic fish. Sci. Adv. *3*, e1602045.

Li, F.X., Shu, J., Zhang, L.R., Yang, N.L., Xie, J., Li, X.P., Cheng, L., Kuang, S.L., Tang, S.Y., Zhang, S.W., et al. (2020). Liquid metal droplet robot. Appl. Mater. Today *19*, 100597.

Li, X.X., Xie, J., Tang, S.Y., Xu, R., Li, X.P., Li, W.H., and Zhang, S.W. (2019). A controllable untethered vehicle driven by electrically actuated liquid metal droplets. IEEE. T. Ind. Inform. *15*, 2535–2543.

Palagi, S., Mark, A.G., Reigh, S.Y., Melde, K., Qiu, T., Zeng, H., Parmeggiani, C., Martella, D., Sanchez-Castillo, A., Kapernaum, N., et al. (2016). Structured light enables biomimetic swimming and versatile locomotion of photoresponsive soft microrobots. Nat. Mater. *15*, 647.

Rafsanjani, A., Zhang, Y.R., Liu, B.Y., Rubinstein, S.M., and Bertoldi, K. (2018). Kirigami skins make a simple soft actuator crawl. Sci. Robot. *3*, eaar7555.

Reichel, K.S., Lozada-Smith, N., Joshipura, I.D., Ma, J.J., Shrestha, R., Mendis, R., Dickey, M.D., and Mittleman, D.M. (2018). Electrically reconfigurable terahertz signal processing devices using liquid metal components. Nat. Commun. *9*, 4202.

Shu, J., Lu, Y.M., Wang, E.L., Li, X.P., Tang, S.Y., Zhao, S.P., Zhou, X.B., Sun, L.N., Li, W.H., and Zhang, S.W. (2020). Particle-based porous materials for the rapid and spontaneous diffusion of liquid metals. ACS Appl. Mater. Interfaces *12*, 11163–11170.

Shu, J., Tang, S.Y., Feng, Z.H., Li, W.H., Li, X.P., and Zhang, S.W. (2018). Unconventional locomotion of liquid metal droplets driven by magnetic fields. Soft Matter *14*, 7113–7118.

Tan, S.C., Gui, H., Yuan, B., and Liu, J. (2015a). Magnetic trap effect to restrict motion of self-powered tiny liquid metal motors. Appl. Phys. Lett. *107*, 071904.

Tan, S.C., Yuan, B., and Liu, J. (2015b). Electrical method to control the running direction and speed of self-powered tiny liquid metal motors. Proc. R. Soc. A. *471*, 20150297.

Tang, S.Y., Khoshmanesh, K., Sivan, V., Petersen, P., O'Mullane, A.P., Abbott, D., Mitchell, A., and Kalantar-zadeh, K. (2014a). Liquid metal enabled pump. Proc. Natl. Acad. Sci. U S A *111*, 3304–3309.

Tang, S.Y., Sivan, V., Khoshmanesh, K., O'Mullane, A.P., Tang, X.K., Gol, B., Eshtiaghi, N., Lieder, F., Petersen, P., Mitchell, A., et al. (2013a). Electrochemically induced actuation of liquid metal marbles. Nanoscale *5*, 5949–5957.

Tang, S.Y., Sivan, V., Petersen, P., Zhang, W., Morrison, P.D., Kalantar-zadeh, K., Mitchell, A., and Khoshmanesh, K. (2014b). Liquid metal actuator for inducing chaotic advection. Adv. Funct. Mater. *24*, 5851–5858.

Tang, X.K., Tang, S.Y., Sivan, V., Zhang, W., Mitchell, A., Kalantar-zadeh, K., and Khoshmanesh, K. (2013b). Photochemically induced motion of liquid metal marbles. Appl. Phys. Lett. *103*, 174104.

Wang, D.L., Gao, C.Y., Wang, W., Sun, M.M., Guo, B., Xie, H., and He, Q. (2018). Shape-transformable, fusible rodlike swimming liquid metal nanomachine. ACS Nano *12*, 10212–10220.

Wang, M., Trlica, C., Khan, M.R., Dickey, M.D., and Adams, J.J. (2015). A reconfigurable liquid metal antenna driven by electrochemically controlled capillarity. J. Appl. Phys. *117*, 194901.

Wu, J., Tang, S.Y., Fang, T., Li, W.H., Li, X.P., and Zhang, S.W. (2018). A wheeled robot driven by a liquid-metal droplet. Adv. Mater. *30*, 1805039.

Xie, J., Li, F., Kuang, S., Yang, H., Li, X., Tang, S., Li, W., and Zhang, S. (2020). Modeling and motion control of a liquid metal droplet in a fluidic channel. Ieee-asme Trans. Mechatron. *25*, 942–950.

Xie, J., Li, F.X., Shu, J., Kuang, S.L., Li, X.P., and Zhang, S.W. (2018). Accurately motion control of a liquid metal droplet in one-dimensional fluidic channel. In 2018 IEEE International Conference on Robotics and Biomimetics (Robio), pp. 934–939.

Xu, S., Yuan, B., Hou, Y., Liu, T.Y., Fu, J.H., and Liu, J. (2019). Self-fueled liquid metal motors. J. Phys. D Appl. Phys. *52*, 353002.

Yang, H., Xu, M., Li, W.H., and Zhang, S.W. (2019). Design and implementation of a soft robotic arm driven by SMA coils. IEEE T. Ind. Electron. *66*, 6108–6116.

Yao, Y.Y., and Liu, J. (2016). Liquid metal wheeled small vehicle for cargo delivery. RSC Adv. *6*, 56482–56488.

Yu, Y., and Miyako, E. (2018). Alternating-magnetic-field-mediated wireless manipulations of a liquid metal for therapeutic bioengineering. iScience *3*, 134.

Zhang, J., Yao, Y.Y., Sheng, L., and Liu, J. (2015). Self-Fueled biomimetic liquid metal mollusk. Adv. Mater. *27*, 2648–2655.

Zhang, N., Shen, P., Cao, Y., Guo, R.F., and Jiang, Q.C. (2019a). Electrically induced spreading of EGaIn on Cu substrate in an alkali solution under wetting and non-wetting conditions. Appl. Surf. Sci. *490*, 598–603.

Zhang, Y.X., Tang, S.Y., Zhao, Q.B., Yun, G.L., Yuan, D., and Li, W.H. (2019b). High-throughput production of uniformly sized liquid metal microdroplets using submerged electrodispersion. Appl. Phys. Lett. *114*, 154101.

iScience, Volume *24*

Supplemental Information

Liquid metal motor

Erlong Wang, Jian Shu, Hu Jin, Zhe Tao, Jie Xie, Shi-Yang Tang, Xiangpeng Li, Weihua Li, Michael D. Dickey, and Shiwu Zhang

Supplemental Materials

Transparent Methods

Liquid metal motor: EGaIn alloy (75% Ga, 25% In) and NaOH was purchased from Sigma Aldrich, USA. The rotor and annular channel of the photopolymer was fabricated by a 3D printer (Formlabs Form2) and the frames of aluminum are fabricated by numerical control (NC) machining system. The DC voltage was provided by a DC power supply (RIGOL DP832). All the electrodes were graphite electrodes (diameter of 2 mm, SMDJ2MM, DENGLIWEI, China). The rotation speed of the motor is measured using a Hall sensor (A1104EUA-T, ALLEGRO, USA).

Electrical brushes rotational friction measurement: The three types of conventional solid-solid contact brushes (H0522-06, M125A-04, SR012-0210A with diameters of 5, 12 and 22 mm, respectively) were purchase from SENRING Electronics, China. The friction was obtained by rheometer (MCR 302, Anton Paar, Austria).

Untethered remote-control vehicle and boat: The bodies of the vehicle and boat were fabricated by 3D printing. The power of the vehicle and boat was provided by a lithium ion battery (PONFLY, 11.1 V). The vehicle was actuated on a glass plate (120 mm × 550 mm) and the boat was actuated in a water tank (200 cm × 60 cm × 60 cm). The use of wireless module (KT117S-4, QIACHIP, China) allows the locomotion of the vehicle and the boat to be controlled remotely.

Videos and photos: Videos were captured using a DSLR camera (5D MARK2, Canon, Japan), and the snapshots were extracted from these videos. The velocity data was obtained using a high-speed camera (HERO 5, GoPro, USA).

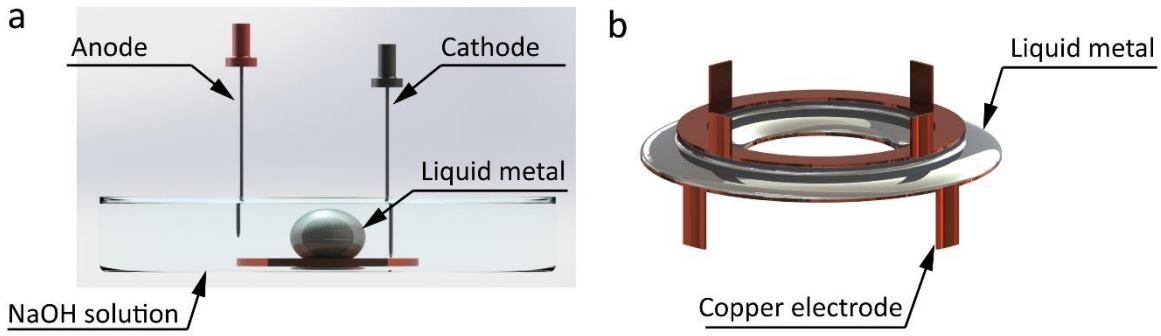

Figure S1. Electrochemical treatment of copper electrodes with liquid metal. Related to Figure 1. (a) Schematic of the electrochemical treatment method. (b) Liquid metal adheres to the two electrode rings after treatment.

We treated the copper surface electrochemically so that liquid metal can wet the surface of copper electrodes. In doing so, we first dropped 50 μL EGaIn on a copper tape in a beaker, and then added 1 mL NaOH solution. We next applied a 10 V DC voltage between the copper tape and the solution to electrochemically wet the surface of copper with liquid metal, as shown in Figure S1a. After the treatment, liquid metal can uniformly cover and adhere to the copper electrode rings on the stator and the rotor, as depicted in Figure S1b.

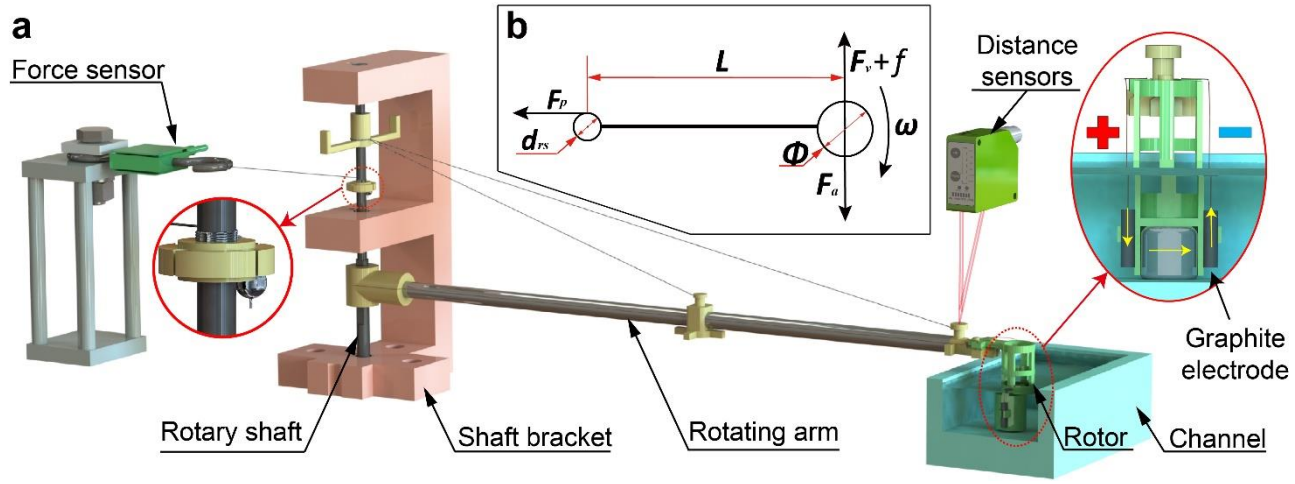

Figure S2. Actuating force measurement system. Related to Figure 3. (a) Schematic of the measuring system. (b) Schematic showing the torque balance of the measuring system. In order to characterize the influence of chamber shape on the thrust, we designed an actuating force measuring system (Figure S2a). We connected the actuating unit to a long rotating arm (1288 mm) for amplifying the torque, and the actuating force was transmitted to the force sensor *via* a polyethylene thread (diameter of 0.165 mm) connected to the rotary shaft. According to the balance of the torque, the actuating force of the chamber F_a can be calculated as:

$$F_a = \frac{F_p \cdot d_{rs}}{2L} - (F_v + f) \quad (1)$$

where F_p is the pulling force of the polyethylene thread which is measured by the force sensor, and d_{rs} and L are the diameter of the rotary shaft and the distance from the chamber to the rotary shaft, respectively (Figure S2b). We fixed the height between the rotor frame and the bottom of the channel to be 0.5 mm, and this distance was monitored using a distance sensor (Figure S2a).

Brackets and connectors in the system are made from aluminum alloy processed by computer numerical control (CNC) machine tools. The force sensor (LSB200, Futek, USA) measures the force on the polyethylene thread and transmits the data to the computer through the data acquisition card (NI-6210). The distance sensor (LK-G30, Keyence, Japan) monitors the height between the bottom of the rotor and the surface of the annular channel.

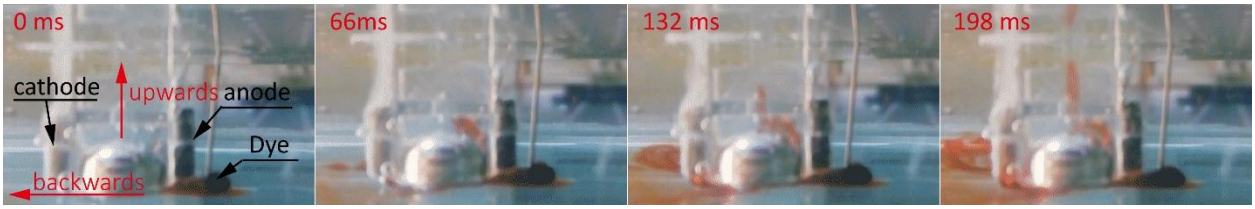

Figure S3. Sequential snapshots of the upward pumping of solution under Marangoni effect. Related to Figure 3. When we apply a DC voltage (9 V) to the graphite electrodes outside the chamber, the continuous electrowetting (CEW) effect induces Marangoni flow on the surface of the liquid metal droplet and can pump the surrounding liquid upwards, as shown in Figure S3. We dropped several orange dye droplets near the anode to indicate the direction of fluid flow.

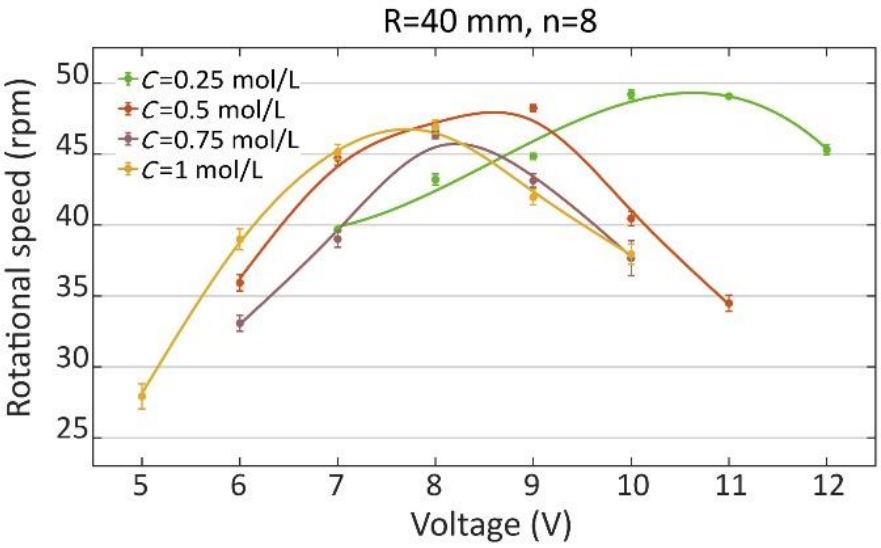

Figure S4. Motor performance with multiple driving units. Related to Figure 3. Plots of no-load speed of liquid metal motor *vs.* voltage; green, brown, purple and yellow curves indicate different concentrations of NaOH solution.

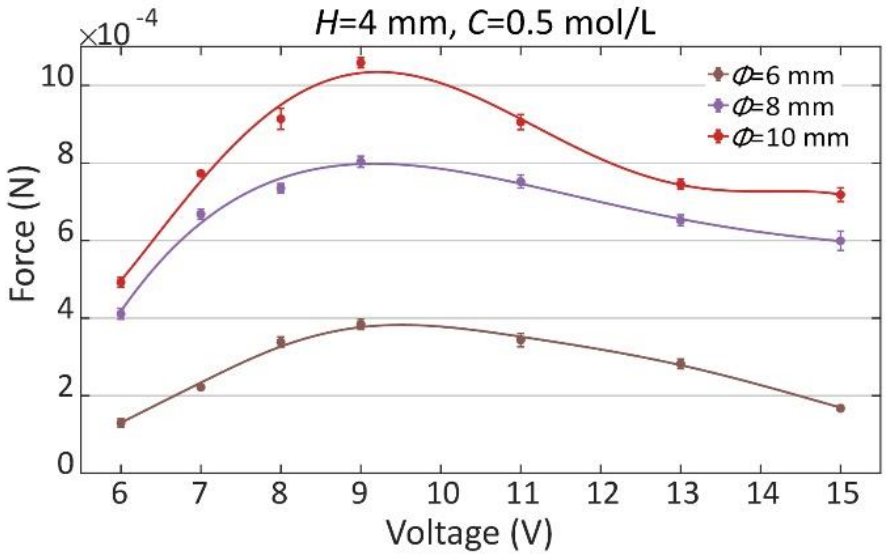

Figure S5. Effect of droplet height H on the actuating force. Related to Figure 3. Plots of driving force of an actuating unit *vs.* voltage; brown, purple and red curves indicate different heights *H* of the liquid metal droplets. We found that droplet with a larger *H* can produce a stronger driving force, which is also in line with Equation (1).